Received: 28 March 2023 | Accepted: 29 September 2023

DOI: 10.1002/vzj2.20290

Vadose Zone Journal

ORIGINAL ARTICLE

Improving evapotranspiration computation with electrical resistivity tomography in a maize field

Chunwei Chou[1] | **Luca Peruzzo**[1,2] | **Nicola Falco**[1] | **Zhao Hao**[1] | **Benjamin Mary**[1,2] | **Jiannan Wang**[1] | **Yuxin Wu**[1]

[1]Lawrence Berkeley National Laboratory, Berkeley, California, USA

[2]Dipartimento di Geoscienze, Università degli Studi di Padova, Padova, Italy

Correspondence
Chunwei Chou, Lawrence Berkeley National Laboratory, 1 Cyclotron Rd, Berkeley, CA 94720, USA.
Email: chunweichou@lbl.gov

Assigned to Associate Editor Helen Dahlke.

Funding information
Lawrence Berkeley National Laboratory; Laboratory Directed Research and Development; U.S. Department of Energy; Office of Science, Grant/Award Number: DE623AC02-05CH11231; Biological and Environmental Research

Abstract

Hydrogeophysical methods have been increasingly used to study subsurface soil–water dynamics, yet their application beyond the soil compartment or the quantitative link to soil hydraulic properties remains limited. To examine how these methods can inform model-based evapotranspiration (ET) calculation under varying soil water conditions, we conducted a pilot-scale field study at an experimental maize plot with manipulated irrigation treatments. Our goal was to develop a workflow for (1) acquiring and inverting field electrical resistivity tomography (ERT) data, (2) correlating ERT to soil hydraulic properties, (3) spatially characterizing soil water stress that feeds into ET modeling (the FAO-56 model), and (4) evaluating the performance of ERT-based ET computation. Our results showed that ERT was able to capture decimeter-scale soil water content (SWC) dynamics from root water uptake and irrigation manipulation and the contrast of soil water stress between deficiently and fully irrigated maize. We also demonstrated the flexibility of using ERT to spatially integrate soil water stress in the soil volume of interest, which could be adjusted based on different crops and plot layouts. The integration of the ERT datasets into ET modeling provided insights into the spatial heterogeneity of the subsurface that has been challenging for point-based sensing, which can further our understanding of the hydraulic dynamics in the soil-plant-atmosphere continuum.

1 | INTRODUCTION

Advancing field-scale soil water content (SWC) mapping tools is critical to improve crop evapotranspiration (ET) computation that requires root zone water availability as a model input. Economic, operational, and ecological objectives such as optimizing irrigation-to-yield ratio, planning for heat and droughts, and transitioning to sustainable practices all seek to increase crop water use efficiency. Quantifying SWC in time and space provides the key information to evaluate when, where, and if the water management scheme needs to be adjusted. Because SWC measurements in the field still largely rely on point sensors, upscaled SWC imaging tools remain desirable, which allows a more holistic evaluation of the extent, severity, and development of soil water stress (Ritchie, 1981). Such data are key to informing irrigation

Abbreviations: DOY, day of year; ER, electrical resistivity; ERT, electrical resistivity tomography; ET, evapotranspiration; ET_o, reference ET; RWU, root water uptake; SDI, subsurface drip irrigation; SMP, soil matric potential; SWC, soil water content.

manipulation, and they are also the often-lacking inputs of hydrological models that estimate ET. Analyzing and predicting how ET is or will be affected by agricultural practices and climate patterns through modeling are also crucial components of water resource management.

One of the widely adopted ET models in the agricultural field is FAO-56, developed by the United Nations Food and Agricultural Organization based on the Penman–Monteith equation (Allen et al., 1998; Monteith, 1965; Penman, 1948). FAO-56 standardizes the calculation of a reference ET (ET_o) from local meteorological observations made above well-watered short grasses, and it includes a library of crop coefficients that correlate ETo to the ET of a great variety of crops, also well-watered, at different growth stages. To quantify the percentage of ET reduced by soil water stress, FAO-56 introduces evaporation (E) and transpiration (T) reduction coefficients as functions of the amount of water remaining in the soil. Because FAO-56 uses a one-dimensional and history-dependent analysis of water fluxes in and out of the root zone to calculate the reduction coefficients, the model assumes spatially homogeneous SWC distribution and root water uptake (RWU) intensity in the rooting depth, generalizing the heterogeneous and depth-dependent root zone water dynamics. Without spatial inputs such as in situ SWC measurements (water source) and the knowledge of where roots actively uptake water (water sink), the derived coefficients could misrepresent the severity of soil water stress that the crop experiences.

Spatial quantification of SWC has been validated using geoelectrical techniques in laboratory and field studies (al Hagrey et al., 2004; Cimpoiaşu et al., 2020). Electrical resistivity tomography (ERT) is one of the methods that characterizes the subsurface with active electrical measurements and inverse modeling (Binley & Kemna, 2005; Ernstson & Kirsch, 2006; Samouëlian et al., 2006), and it has produced soil electrical resistivity (ER) maps that were sensitive to SWC distribution (Kelly et al., 2011; Michot et al., 2001; Panisodd et al., 2001). Because current flow in the soil depends on pore water connectivity (Bussian, 1983), pedophysical relationships between soil ER and SWC could be established. These soil-specific calibrations have been tested in situ with embedded arrays of time-domain reflectometry (TDR) sensors (Beff et al., 2013; Michot et al., 2003; Werban et al., 2008) and neutron probes (Srayeddin & Doussan, 2009), and ex situ with laboratory pedophysical experiments (Celano et al., 2011; Zhou et al., 2001). Petrophysical models such as Archie and Archie-like formulations have been adopted to describe the soil ER–SWC correlation (Archie, 1942).

Vadose zone hydrological processes have been investigated by analyzing the temporal and spatial variation in SWC from the ERT monitoring datasets. Time-lapse ERT helped visualize SWC dynamics such as RWU (Mary et al., 2020; Michot et al., 2001), irrigation drainage (Kelly et al., 2011), and preferential water infiltration via root channels (Beff et al., 2013; Zhou et al., 2001). At an hourly timescale, ERT monitoring also captured the diurnal trends of transpiration and SWC redistribution (Blanchy et al., 2020; Werban et al., 2008). Agricultural practices that contribute to the spatial heterogeneity of SWC were also surveyed using ERT, including deficient irrigation (Srayeddin & Doussan, 2009; Vanella et al., 2021), soil compaction from machinery, tillage, and pasturage (Losinno & Sainato, 2018; Michot et al., 2003), and cover crop rotation (Celano et al., 2011). Several studies also used ERT to compute agricultural variables such as plant available water (Brillante et al., 2016), water depletion rate (Garré et al., 2011), and SWC mass balance (Cassiani et al., 2012; Celano et al., 2011) by analyzing the changes of soil ER over time. To the best of our knowledge, ERT has only been coupled with the FAO-56 model once to improve the estimation of the fraction of wet and exposed soil surface and thus the evaporation from soil (Vanella et al., 2019), while the calibration of FAO-56 ET reduction coefficients using ERT has not been investigated.

We conducted a field study in a conventional maize plot in Davis, CA, where ET was supplied with controlled subsurface drip irrigation (SDI). Our goals were to (1) investigate ERT's capability of resolving decimeter SWC variations resulting from contrasting irrigation regimes and RWU patterns and (2) integrate ERT-based SWC characterization into ET computation, such as daily ET based on the United Nations Food and Agricultural Organization ET model (FAO-56) (Allen et al., 1998) and accumulative ET through SWC mass balance.

Core Ideas

- Electrical resistivity tomography (ERT) captured soil water dynamics induced by root water uptake and irrigation manipulation.
- ERT enabled spatial analysis and quantification of soil water stress, a key input to the evapotranspiration (ET) model.
- A workflow from field ERT data acquisition to ET computation was demonstrated.

2 | MATERIALS AND METHODS

2.1 | Field site and experiment timeline

The field experiment was carried out at Russell Ranch Sustainable Agriculture Facility in Davis, CA (38°32′32.9″N,

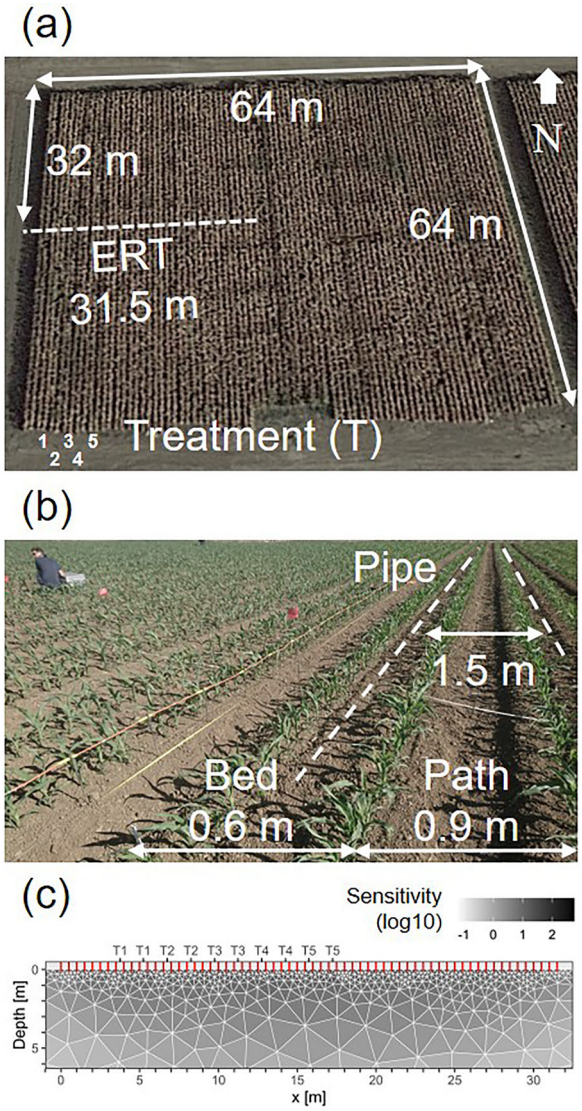

FIGURE 1 Corn plot images. (a) A bird-eye view of the plot from Google Earth. The five treatments of interest (T1–T5) at the west end of the plot are labeled, and the dotted line denotes the cross-sectional electrical resistivity tomography (ERT) transect perpendicular to the beds at the N-S midpoint. (b) The layout of the row crop field—alternating irrigated beds with subsurface drip irrigation pipelines (dotted lines) and nonirrigated paths. (c) Positions of the 64, 0.5-m spaced ERT electrodes (red bars) along the ERT transect and the sensitivity of two-dimensional ERT data in the depth (6 m) of investigation.

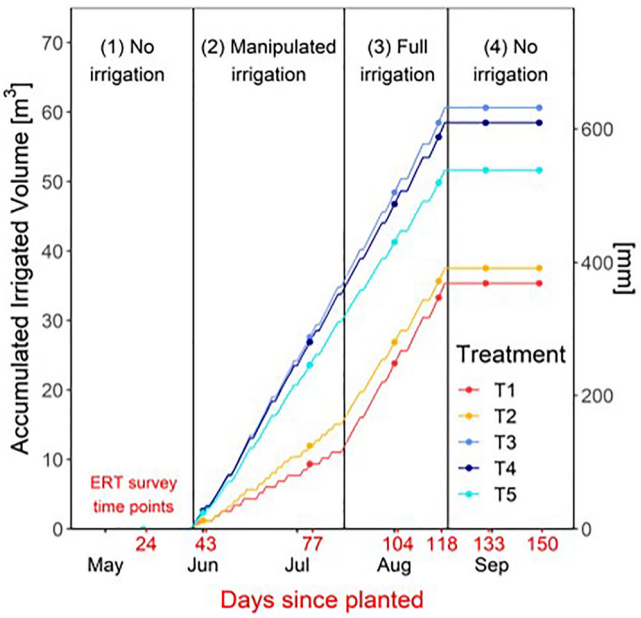

FIGURE 2 Accumulated irrigated volume per bed. The equivalent unit in millimeter was calculated as volume (m^3) divided by interbed area (1.5 × 64 m^2). Four stages of irrigation and 7 days of electrical resistivity tomography (ERT) surveys (in red) are also labeled.

121°52′32.0″W). *Zea mays* (maize) was seeded in a row crop field (64 × 64 m^2) at a density of 80,000 plants ha^{-1} on April 21, 2018, and harvested on October 5, 2018 (Figure 1a). To compensate for the lack of precipitation (7.4 mm during the experiment duration) and low water table (12-m deep on March 21, 2018, and 21-m deep on October 4, 2018) during the growing season, groundwater was pumped and supplied to every two rows (one bed) of maize via SDI pipelines buried at 0.1-m depth (Figure 1b). The timeline of irrigation was divided into four stages: (1) no irrigation (day of year [DOY] 111–148), (2) manipulated (deficit) irrigation (149–196), (3) full irrigation (197–229), and (4) no irrigation (230–278) (Figure 2). On each day of irrigation, the water was delivered at an average rate of 1 mm h^{-1} for 8 h for both full and deficit irrigation (between 0630 and 1430 PST).

In this study, we focused on the 10 beds at the west end of the plot, excluding two beds at the edge where maize was visually undersized (Figure 1a). Among the 10 beds, five levels of water or nitrogen stress treatments (T1–T5) were applied to five pairs of adjacent beds (Table 1). At T1–T2, manipulated deficit irrigation, an irrigation-to-yield optimizing strategy, was adopted, where water was limited to the maize before the drought-sensitive growth stages. During the manipulated irrigation stage, the irrigation system was activated for 2 (T1), 3 (T2), or 6 (T3–T5) days per week, followed by the full irrigation stage when all treatments received 6 days of irrigation per week to ensure kernel development during the maize reproductive stages (silk and grain filling) (Figure 2).

The soil at the facility was classified as Alfisol Haploxeralf—clay-rich, minimally stratified, and wet in winters—under USDA's taxonomy. Wolf et al. (2018) showed that the plot had a similar particle size distribution from 0- to 2-m depth with an average of 22% sand, 57% silt, and 21% clay (silt loam) (Table 2), and overall the mean dry bulk density gradually increased with depths (Table 3). Soil organic matter was 1.8% lost upon ignition.

TABLE 1 Details of the water and nitrogen stress treatments.

Treatment	Irrigation[a] (mm week^{-1})	Nitrogen fertilizer (kg ha^{-1})	Stress type and level
T1	16	235	Water, high stress
T2	24	235	Water, medium
T3	48	119	Nitrogen, medium
T4	48	235	Control
T5	48	27	Nitrogen, high

[a]The irrigation volume during the manipulated irrigation stage.

TABLE 2 Soil particle size distribution data at the maize plot extracted from Wolf et al. (2018).

Depth (m)	Year[a]	Sand (%)	Silt (%)	Clay (%)	Texture
0.00–0.15	1993	21	61	18	Silt loam
	2012	18	61	21	Silt loam
0.15–0.30	1993	18	61	21	Silt loam
	2012	17	60	23	Silt loam
0.30–0.60	1993	17	61	22	Silt loam
	2012	19	59	22	Silt loam
0.60–1.00	1993	24	54	22	Silt loam
	2012	36	47	17	Loam
1.00–2.00	1993	22	60	18	Silt loam
	2012	18	61	21	Silt loam

[a]In 1993, 10 samples from each depth across the 1-acre plot were compiled together for the analysis. In 2012, six samples were compiled. See Wolf et al. (2018) for analysis details.

2.2 | Workflow

Our proposed workflow from field ERT data acquisition to ET computation is summarized in Figure 3. Note that the figures, tables, and equations that will be discussed in the future sections are included here for future reference. In short, ERT was converted into ET reduction coefficients based on laboratory pedophysical experiments, and a spatial analysis of the coefficients was performed to generate model input to calculate daily ET. Time-lapse differences in ERT, together with the irrigation data, were also used to compute accumulative ET.

2.3 | ERT data acquisition and inversion

Throughout the growing season, we acquired seven ERT surveys on DOY 134 (no irrigation), 153 and 187 (manipulated irrigation), 214 and 228 (full irrigation), and 243 and 260 (no irrigation). On each day of acquisition, we laid down a 31.5-m long ERT transect, crossing the 10 beds of interest perpendicularly at their N-S midpoint (Figure 1a,c). Sixty-four stainless steel electrodes were installed at 0.05-m deep with a 0.5-m inter-electrode spacing, and the position of the electrodes was kept consistent across acquisition by using a cable with a fixed 0.5-m lead spacing and referring to flags we set in place along the transect (Figure 1c). The ERT system in use was MPT-DAS-1 (Multi-phase Technology). Our acquisition followed a skip-2 dipole–dipole sequence with 1284 reciprocal pairs of electrode configurations, where the same responses are expected when the pairs of electrodes used for injection and measurement are interchanged (Parasnis, 1988). The measurements were taken in the time domain at the base frequency of 1 Hz, target voltage of 200 V, target current of 2 A, and stacking of 3.

Before the inversion, ERT data with high reciprocal errors (>5%), stacking errors (>5%), apparent resistivity (>1000 Ωm), electrode contact resistance (>30,000 Ω), and/or low voltages (absolute value < 0.0005 V) were excluded. On average, 84% of the data were retained, ranging from 65% to 99% depending on the data quality of each acquisition. Each time step was then inverted independently using pyGIMLI processing codes (Rücker et al., 2017), aiming at a smoothed inversion of the apparent resistivity data while minimizing the data misfit (0.8 < chi-squared < 1.2). Time-lapse constraints were not applied in the inversion due to dynamic and competing processes such as irrigation and ET in this open system, which does not guarantee sequential changes among acquisitions at $t-1$, t, and $t+1$. The inverted resistivity (ρ_T [Ω m]) was adjusted to 25°C (ρ [Ω m]) based on the soil temperature (T [°C], ranging between 16 and 24 °C during the growing season) measured and interpolated among depths (0.1, 0.25, 0.5, 1, 2, and 5 m) (Hayashi, 2004):

$$\rho_T = \rho\,[1 + 0.02\,(T - 25)] \quad (1)$$

2.4 | Laboratory pedophysical experiments

2.4.1 | Soil electrical experiment

To correlate soil-specific electrical and hydraulic properties, we measured soil ER and soil matric potential (SMP) across a wide range of saturation degrees in the lab. Soil ER was measured in a cylindrical polyvinyl chlroide (PVC) column (inner diameter 0.145 m, height 0.05 m), in which the topsoil (0–0.25 m) sampled from the field using the direct push method

TABLE 3 Dry bulk density data at the maize plot extracted from Wolf et al. (2018).

Depth (m)	Number of samples	Dry bulk density[a] (g cm^{-3})	Porosity[b] (m^3 m^{-3})
0.00–0.15	16	1.34 ± 0.16	0.494 ± 0.059
0.15–0.30	12	1.35 ± 0.23	0.489 ± 0.085
0.30–0.60	14	1.46 ± 0.10	0.451 ± 0.038
0.60–1.00	8	1.50 ± 0.10	0.435 ± 0.039
1.00–1.50	6	1.49 ± 0.18	0.440 ± 0.067
1.50–2.00	6	1.55 ± 0.13	0.415 ± 0.035

[a]Mean ± standard deviation among the number of samples acquired across the 1-acre plot in 1992, 1995, 1999, 2003, 2007, and 2012. See Wolf et al. (2018) for analysis details.

[b]Porosity is calculated as 1 − dry bulk density/soil particle density (taken as 2.65 g cm^{-3}).

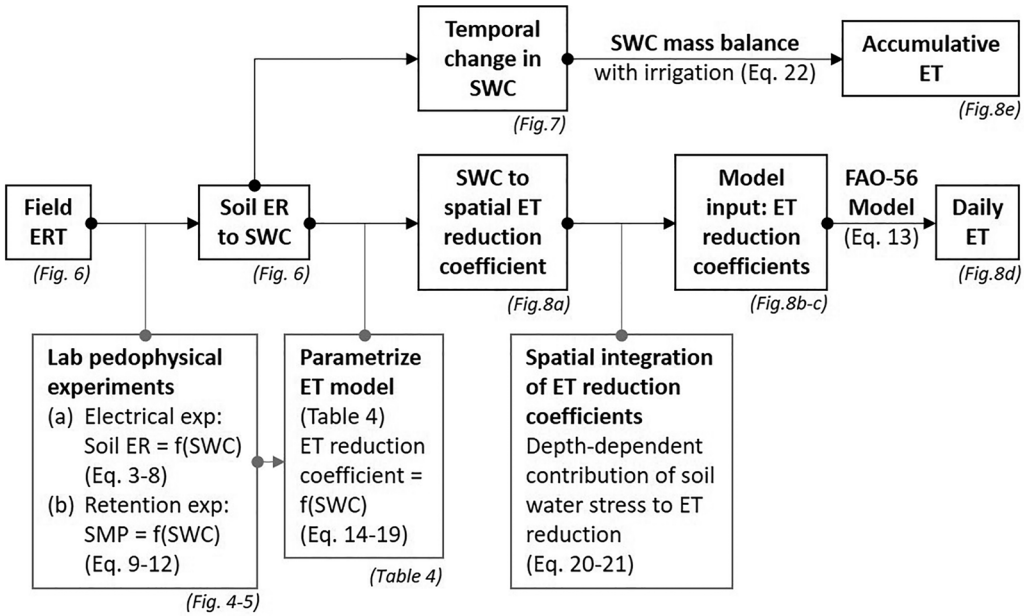

FIGURE 3 Summary of the workflow. ER, electrical resistivity; ERT, electrical resistivity tomography; ET, evapotranspiration; SMP, soil matric potential; SWC, soil water content.

was repacked with a pestle (Figure 4a). We installed two four-electrode arrays (a total of eight Ag/AgCl electrodes) from the bottom of the column, where the two outer electrodes were used to inject current, and the inner pair measured the soil resistance (PSIP, Ontash & Ermac). Resistivity was calculated from resistance using the geometric factors determined with solutions of known conductivity (Figure 4b). To saturate the soil, we placed the soil column in the water obtained from the field, and the water was only allowed to flow upward into the soil via openings drilled from the bottom of the column to avoid trapping air. The bottom-up saturation process lasted 2 weeks until the soil surface appeared glossy, and the SWC estimate exceeded 0.41, a value obtained from the water retention experiment described in the following section. During the experiment, water loss was only allowed via evaporation from the top, and the SWC (θ [m^3 m^{-3}]) and saturation degree (S [m^3 m^{-3}]) at each acquisition were determined gravimetrically and eventually via oven-drying at 60°C until the weight stabilized (porosity [φ] = 0.453 and dry bulk density = 1.46 g cm^{-3}):

$$S = \frac{\theta}{\varphi} \tag{2}$$

Soil ER was corrected to 25°C (ρ [Ω m]) and saturation degree (S) data were fitted using the Waxman–Smits model (Waxman & Smits, 1968):

$$\rho = \varphi^{-M} S^{-N} \left(\frac{1}{\rho_f} + \frac{bQ_v}{S} \right)^{-1} \tag{3}$$

$$\log(\rho) = -M \log(\varphi) - N \log(S) - \log\left(\frac{1}{\rho_f} + \frac{bQ_v}{S} \right) \tag{3a}$$

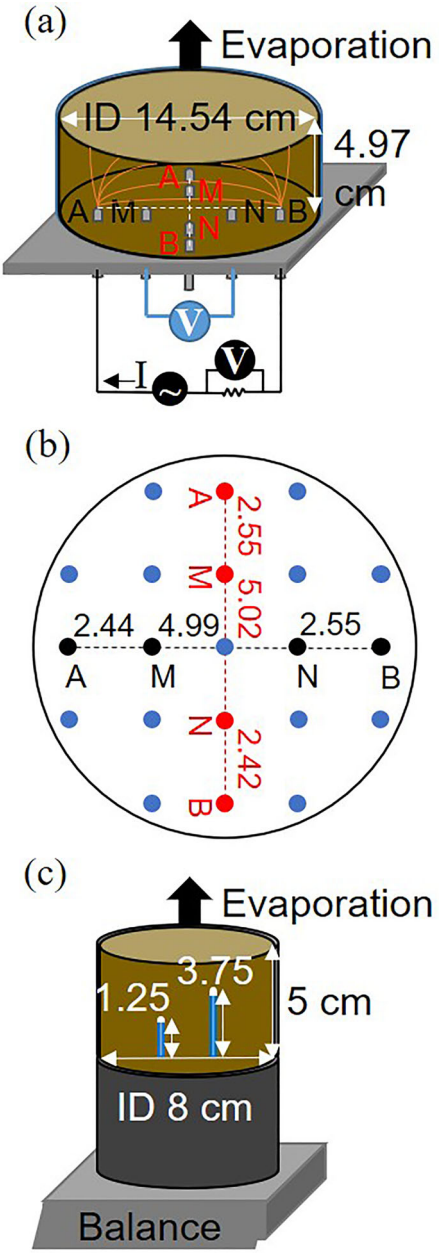

FIGURE 4 Pedophysical experiments: Soil electrical characterization. (a) Electrodes (A, B) were used for injecting current and (M, N) for measuring resistance. (b) From the bottom of the column: the location of the two electrode arrays (black and red, spacing in [cm]) and the openings for saturating the soil (blue). (c) Water retention analysis. The tensiometers at two heights measured soil matric potential (SMP), and the balance monitored soil water content (SWC) gravimetrically. ID, inner diameter.

$$b = 3.83\left(1 - 0.83e^{-\frac{0.5}{\rho_f}}\right) \tag{4}$$

$$Q_v = \mathrm{CEC} \times D_{soil} \times \frac{1-\varphi}{\varphi} \tag{5}$$

where φ ($m^3\ m^{-3}$) is the porosity, ρ_f ($S\ m^{-1}$) is the pore water resistivity, b ([$S\ m^{-1}$]/[meq cm^{-3}]) is the equivalent ionic conductance of exchange cations, Q_v (meq cm^{-3}) is the cation exchange capacity per unit pore volume, CEC (meq g^{-1}) is the cation exchange capacity (taken as 0.2529, measured by Blundell et al., 2020), and D_{soil} (g cm^{-3}) is the soil particle density (taken as 2.65). The model parameters, M [−] (cementation exponent) and N [−] (saturation exponent), were fitted with linear regression using the log-log form of the Waxman–Smits model (Equation 3a). The saturation-dependent pore water resistivity (ρ_f) was estimated following Hilhorst (2000):

$$\rho_f = \rho\frac{\varepsilon - \varepsilon_s}{\varepsilon_w} \tag{6}$$

where ε_w (−) is the dielectric permittivity of the water (taken as 78.5 at 25°C), ε_s (−) is the dielectric permittivity of the dry soil (taken as 4.1, Hilhorst, 2000), and ε (−) is the dielectric permittivity of the bulk soil, solved using Topp Equation (Topp et al., 1980):

$$\theta = -5.3\times10^{-2} + 2.92\times10^{-2}\varepsilon - 5.5\times10^{-4}\varepsilon^2 + 4.3\times10^{-6}\varepsilon^3 \tag{7}$$

Finally, an empirical model was fitted to generalize pore water resistivity (ρ_f) as a function of saturation degree (S):

$$\log(\rho_f) = \log(\rho_{fsat}) + c\log(S) \tag{8}$$

where $\rho_{f\,sat}$, ($S\ m^{-1}$) pore water resistivity at full saturation, and c (−), an empirical exponent, were fitted linearly using the estimated pore water resistivity (Equations 6 and 7) and the measured saturation.

2.4.2 | Soil water retention experiment

SMP was measured in a Hyprop unit (METER). Adjacent to the soil sample used for the electrical measurements, a cylindrical soil sample was cored from the field at 0.05- to 0.1-m depth and saturated with the irrigation water initially using the aforementioned bottom-up saturation technique. As the soil dried, SMP was measured and calculated as the geometric mean between the two tensiometer readings, and SWC was monitored gravimetrically with the balance and determined via oven-drying at 60°C until the weight stabilized eventually (porosity = 0.407 and dry bulk density = 1.56 g cm^{-3}) (Figure 4c). Additional SMP of drier soil (<−880 hPa) was measured using WP4C (METER), which calculated the SMP of the sample by measuring its dew point temperature. The SMP and saturation degree data were fitted with a PDI variant

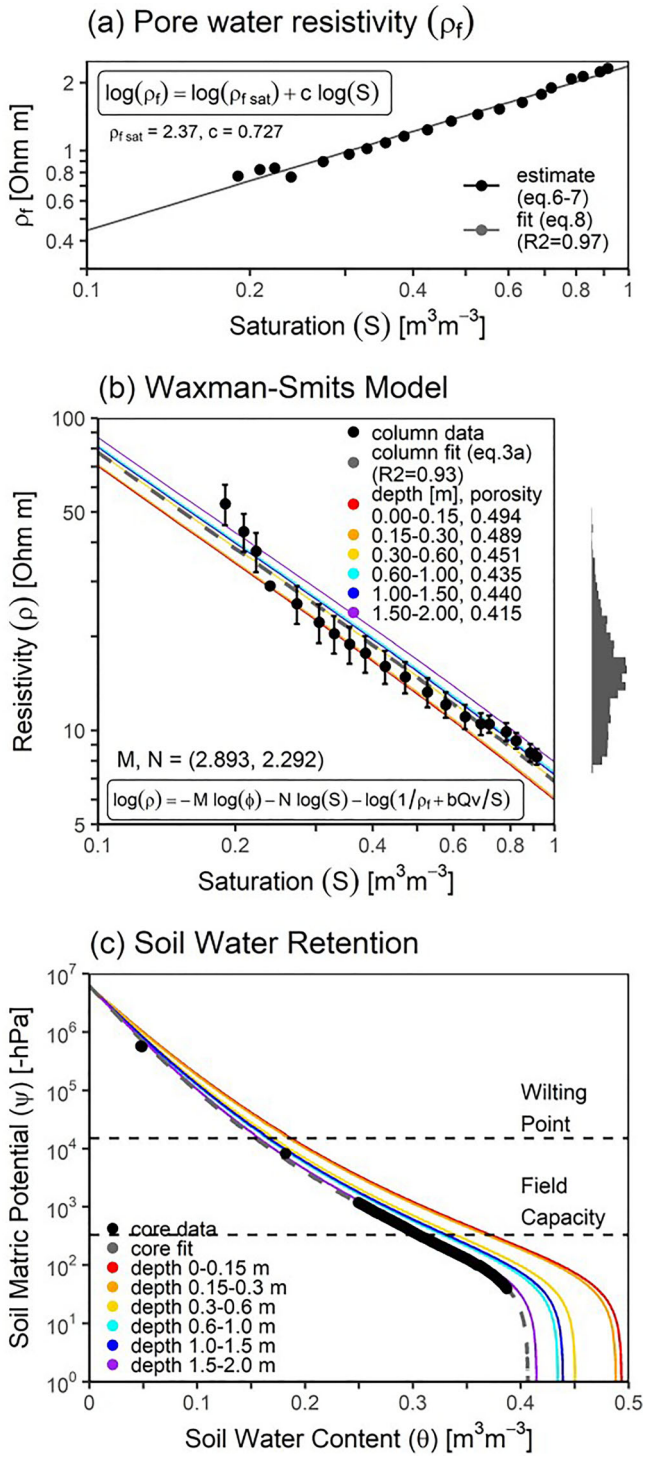

FIGURE 5 Soil electrical–hydraulic relationship. (a) Empirical relationship between saturation degree and pore fluid resistivity. (b) Waxman–Smits model. The error bar is the standard deviation from multiple acquisitions at a single soil water content (SWC) during the laboratory experiment, and the colored lines show the calibration relationship at each depth with different porosity input. The histogram to the right is the distribution of the field resistivity values between 0- and 2-m depth from all field campaigns. (b) Soil water retention curve. Field capacity is at −330 hPa and wilting point at −15,000 hPa, and the colored lines show the retention curve at each depth with different porosity input.

(Iden & Durner, 2014; Peters, 2013) of the unimodal constrained (van Genuchten model, 1980) using the Hyprop-Fit software:

$$S(\psi) = \left(1 - S_{res}\right) s^{cap}(\psi) + S_{res} s^{ad}(\psi) \tag{9}$$

where S ($m^3\ m^{-3}$) is the saturation degree, ψ (hPa) is the SMP, and S_{res} is the saturation degree at maximum SWC of adsorptive water. The retention curve parameters, α (cm^{-1}) (the inverse of the soil suction at air entry of the adsorptive retention) and n (−) (a curve shape parameter), are embedded in the formulation of the two saturation functions: capillary (s^{cap}) and adsorptive saturation function (s^{ad}) (Pertassek et al., 2015):

$$s^{cap}(\psi) = \frac{\left[\frac{1}{1+(-\alpha\psi)}\right]^{1-\frac{1}{n}} - \left[\frac{1}{1+(-\alpha\psi_o)}\right]^{1-\frac{1}{n}}}{1 - \left[\frac{1}{1+(-\alpha\psi)}\right]^{1-\frac{1}{n}}} \tag{10}$$

$$s^{ad}(\psi) = 1 + \frac{1}{\log\left(\frac{1}{\alpha}\right) - \log(-\psi_o)} \left\{ \log(-\psi) - \log\left(\frac{1}{\alpha}\right) + d\ln\left[1 + e^{\frac{\log\left(\frac{1}{\alpha}\right) - \log(-\psi)}{d}}\right]\right\} \tag{11}$$

$$d = 0.1 + \frac{0.2}{n^2}\left[1 - e^{-\left(\frac{S_{res}}{1-S_{res}}\right)^2}\right] \tag{12}$$

A distinction of the PDI model is that it forces the soil suction to reach oven-dryness at $\psi_o = -10^{6.8}$ hPa when SWC = 0 (Schneider & Goss, 2012). The parameters α, n, and S_{res} were fitted by minimizing the residual sum of squares.

2.5 | Evapotranspiration

2.5.1 | Reference ET model

In this study, we used the dual crop coefficient model from FAO-56 as our reference model:

$$ET_{c\,adj} = ET_o\left(K_e + K_{cb}S_S\right) \tag{13}$$

where $ET_{c\,adj}$ (L/T) is the adjusted crop ET for nonoptimal conditions, ET_o (L/T) is the reference ET over a well-watered grass surface, K_e (−) is the soil evaporation coefficient, K_{cb} (−) is the basal crop coefficient (for transpiration), and K_s (−)

is the water stress coefficient (for transpiration). ET_o is a standardized measurement available in most weather stations, and we acquired ours from a station managed by the California Irrigation Management Information System, 9 km away from the maize plot. K_e depends on the irrigation method, crop coverage, and water availability in the topsoil; K_{cb} depends on the species, crop development, and local climate; K_s depends on the species and water availability in the root zone. The derivation of K_{cb}, K_e, and K_s can be found in FAO-56 Chapters 7 and 8 (Allen et al., 1998).

2.5.2 | ET reduction coefficients

FAO-56 uses two ET reduction coefficients to quantify the decrease of evaporation (E) and transpiration (T) rate as the soil dries: K_r (soil evaporation reduction coefficient, embedded in the calculation of K_e) and K_s, where K_r and K_s are the ratios of the actual E and T to their optimal rates, respectively. FAO-56 defines three stages of reduction: (1) Optimal ET ($K = 1$): when field capacity is reached after a significant precipitation or irrigation event, there is readily evaporable water in the evaporative depth (Z_e) and plant-available water in the effective rooting depth (Z_r) for ET without limitation. (2) Reduced ET ($1 < K < 0$): when the readily evaporable/available water is depleted, the rate of E or T decreases from its optimal rate as the SMP decreases. (3) ET Ceases ($K = 0$): strong adsorption between soil matrix and water inhibits E or T when total evaporable or available water is depleted (see fig. 38 and 42 in Allen et al., 1998).

Computing ET reduction coefficients as a function of the cumulative depletion of soil water requires quantifying and balancing the water influxes (irrigation, precipitation, and capillary rise) and effluxes (ET, surface runoff, and deep percolation). Several limitations arise with this approach: (1) subsurface fluxes are difficult to quantify; (2) ET, the final output, feeds into the computation of K_r and K_s; (3) the assumption that the soil is at field capacity homogeneously after rain or irrigation can be invalid; (4) reducing the soil volume to one dimension ignores the spatial distribution of SWC and roots. To address these challenges, we reformulated the reduction coefficient (K_r and K_s) equations from functions of cumulative depletion to functions of SWC (θ):

$$\theta_{FC} = S\left(\psi = -330\text{hPa}\right)\varphi \tag{14}$$

$$\theta_{WP} = S\left(\psi = -15,000\text{hPa}\right)\varphi \tag{15}$$

$$\theta_{K_r} = \theta_{FC} - \left[3.121\left(\theta_{FC} - 0.5\theta_{WP}\right)\Delta z + 0.229\right] \tag{16}$$

$$\theta_{K_S} = \theta_{FC} - p\left(\theta_{FC} - \theta_{WP}\right) \tag{17}$$

$$K_r(\theta) = \begin{cases} 1, \theta \geq \theta_{K_r} \\ \frac{\theta - 0.5\theta_{WP}}{\theta_{K_r} - 0.5\theta_{WP}}, \theta_{K_r} > \theta > 0.5\theta_{WP} \\ 0, 0.5\theta_{WP} > \theta \end{cases} \tag{18}$$

$$K_r(\theta) = \begin{cases} 1, \theta \geq \theta_{K_S} \\ \frac{\theta - \theta_{WP}}{\theta_{K_S} - \theta_{WP}}, \theta_{K_S} > \theta > \theta_{WP} \\ 0, \theta_{WP} > \theta \end{cases} \tag{19}$$

where θ_{FC} ($m^3\ m^{-3}$) is the SWC at field capacity (using Equation 9), θ_{WP} ($m^3\ m^{-3}$) is the SWC at wilting point (using Equation 9), θ_{Kr} ($m^3\ m^{-3}$) is the SWC below which the evaporation rate is reduced ($K_r < 1$), and θ_{Ks} ($m^3\ m^{-3}$) is the SWC below which the transpiration rate starts to decrease ($K_s < 1$). The reduction coefficients are a function of Δz (m) (effective evaporative depth, taken as 0.1 m, eq. 73 in Allen et al., 1998) or p (−) (a crop-specific soil water depletion fraction before the roots start to experience water stress, taken as 0.55 for maize, tab. 22 in Allen et al., 1998). This SWC-based approach does not require temporal fluxes as inputs, and it allows spatial analysis of soil water stress when spatial SWC characterization is available. In alignment with FAO-56, our water stress analysis was only concerned with soil drier than field capacity, and therefore the hypoxic condition was not discussed.

2.6 | Hydrogeophysical methods in ET computation

ERT and the pedophysical relationship were introduced into ET computation through (1) calculating the ET reduction coefficients for the daily FAO-56 dual crop coefficient model and (2) quantifying accumulative ET based on SWC mass balance from ERT time lapse. The first step of both methods involved converting soil ER from ERT to SWC based on the laboratory pedophysical relationship. Several assumptions were made to bridge laboratory results to field application: (1) model parameters—M and N in Waxman–Smits (Equation 3a), $\rho_{f\,sat}$ and c in pore fluid resistivity (Equation 8), and α, n, and S_{res} in van Genuchten (Equations 9–12)—were taken as the fitted values from the column experiments; (2) CEC and soil particle density were set constant (Equation 5); (3) porosity of the soil at the field was treated as a depth-dependent input (Table 3), which was used to (a) convert saturation degree derived from ERT into SWC (Equations 3a and 5), (b) determine SWC at field capacity and wilting point (Equations 14 and 15), and (c) calculate SWC thresholds where

TABLE 4 Soil water content thresholds derived from the lab experiment and calculated for the field application at different depths.

	Saturated (porosity) (φ)	Field capacity (θ_{FC})	Reduced transpiration (θ_{Ks})	Reduced evaporation (θ_{Kr})	Wilting point (θ_{WP})
Lab experiment	0.407	0.310	0.225	0.212	0.153
Field (depth, [m])					
0.00–0.15	0.494	0.373	0.271	0.263	0.188
0.15–0.30	0.489	0.369	0.268	0.260	0.186
0.30–0.60	0.451	0.341	0.248	0.238	0.171
0.60–1.00	0.435	0.329	0.239	0.229	0.165
1.00–1.50	0.440	0.332	0.241	0.232	0.167
1.50–2.00	0.415	0.314	0.228	0.217	0.158

E/T is reduced (Equations 16 and 17). After the SWC (θ_i) of each ERT mesh cell (i) was determined, we calculated local ET reduction coefficients (k_{ri} and k_{si}) at each cell (Equations 18 and 19), which were finally integrated spatially as weighted averages to be the inputs to FAO-56 model ($K_{r\,ERT}$ and $K_{s\,ERT}$):

$$K_{r\,ERT} = \frac{\sum k_{ri} w_i}{\sum w_i} \tag{20}$$

$$K_{S\,ERT} = \frac{\sum k_{si} w_i}{\sum w_i} \tag{21}$$

where w_i (−) is the weight given to each cell based on their contribution to ET.

For transpiration (w_i), the soil underneath the nonirrigated paths and/or deeper than the effective rooting depth (Z_r), where RWU was insignificant, received $w = 0$. The effective rooting depth was estimated as a function of growth days based on nonlocal field measurements of maize (Archontoulis & Licht, 2017). They observed a root growth rate of 7 mm day^{-1} before the fifth-leaf stage (DOY 131 at our plot), followed by 31 mm day^{-1} until the silking stage, when the maximum depth of ∼1.5 m was reached (DOY 175 at our plot). Within the root zone, the weight was assigned as a function of depth, w(z), according to a 4-3-2-1 rule proposed by Kranz et al. (2008), where the maize roots in the top quarter of the rooting depth contribute to 40% of the total water uptake ($w = 0.4$), second quarter to 30% ($w = 0.3$), third quarter to 20% ($w = 0.2$), and the bottom quarter to 10% ($w = 0.1$).

For evaporation (w_i), the soil deeper than the effective evaporative depth ($\Delta z = 0.1$ m), where E was insignificant, was assigned $w = 0$, because the residual diffusive evaporation below Δz is incorporated into K_{cb} and therefore governed by Ks (Equation 13; Aleen et al., 1998). The topsoil was assumed to contribute uniformly to E ($w = 1$), which could be adjusted based on canopy coverage. No depth-dependent weight was assigned to k_{ri} because we did not intend to resolve the vertical differences within Δz using the 0.5-m spaced electrodes.

To calculate accumulative ET (ET_{acc}), we subtracted two consecutive ERT to obtain the changes in SWC at the top 2 m (ΔSWC). Capillary rise and deep percolation beyond 2 m were neglected, assuming that the SDI system was efficient (Ayars et al., 1999). ET_{acc} between the two surveys was calculated as:

$$ET_{acc} = \text{Irrigation} - \Delta\text{SWC} \tag{22}$$

3 | RESULTS AND DISCUSSION

3.1 | Soil electrical-hydraulic calibration

The relationship between saturation degree and soil ER was fitted with the Waxman–Smits model ($M = 2.893$; $N = 2.292$), saturation and pore water resistivity with an empirical relationship ($\rho_{f\,sat} = 2.37\ \Omega$ m; $c = 0.727$), and saturation potential and SMP with the van Genuchten model ($\alpha = 0.0143$; $n = 1.247$; $S_{res} = 0.523$) (Figure 5a–c). The figures also show the depth-dependency of these relationships when the mean porosity at each depth (Table 3) was fed into the functions to apply the calibration on the field data. The SWC thresholds at field capacity, reduced E/T, and wilting point at each depth were calculated and summarized in Table 4, and the equivalent SMP was around −2200 hPa at reduced T (θ_{Ks}) and between −2850 and −2590 hPa at reduced E (θ_{Kr}).

3.2 | Soil water dynamics

Time-lapse ERT and the pedophysical relationship were applied to obtain the spatial distribution and temporal changes of SWC at the maize plot. Here, we focused on the top 2-m depth where ERT data coverage and resolution were higher, ET was active, and soil particle size distribution was

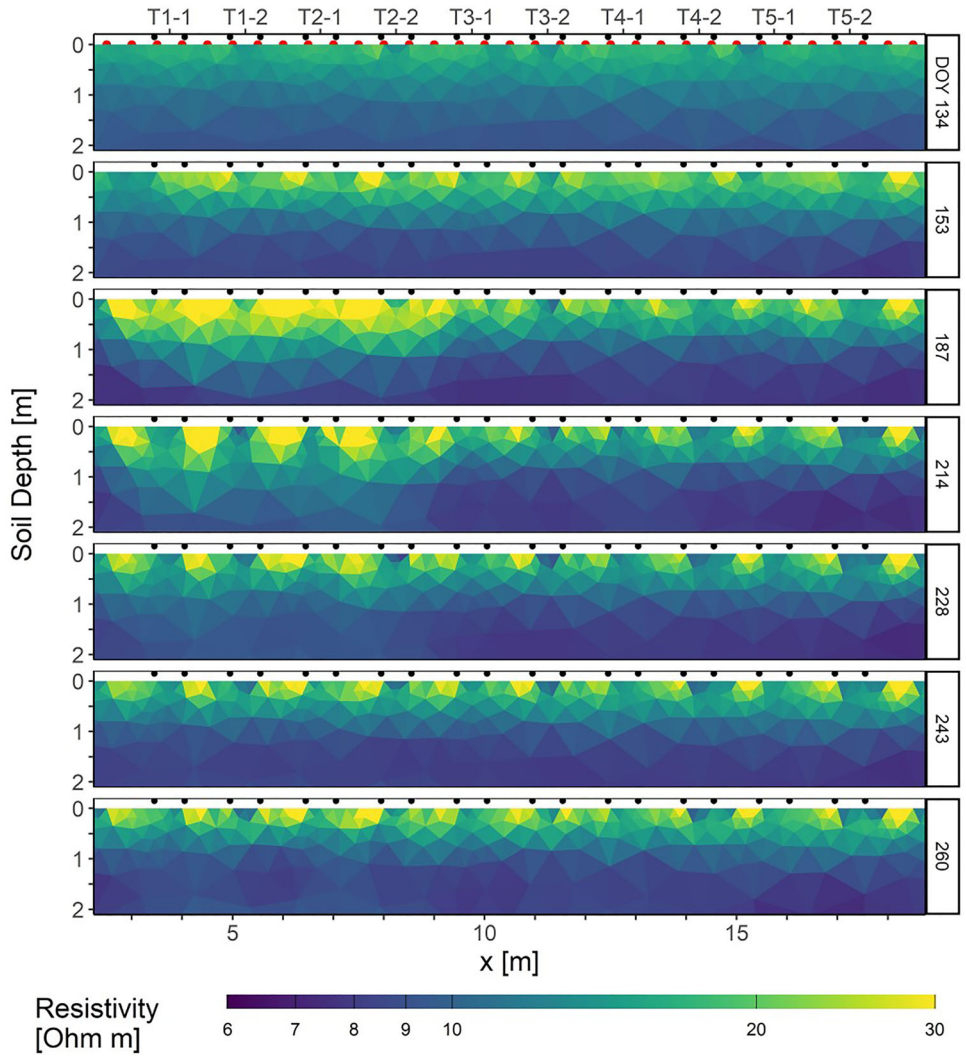

FIGURE 6 Time-lapse electrical resistivity tomography (ERT) between 0- and 2-m depth. The center (i.e., the SDI pipelines) of the 10 beds of interest, each including two rows of maize (black dots), are marked with the treatment and the replicate number, and the positions of the electrodes (red dots) are labeled on day of year (DOY) 134.

similar, which led to the assumption of the applicability of the laboratory-fitted model parameters in the homogeneous soil.

The surface ERT array was able to distinguish decimeter-scale contrasts in the irrigated row crop system (Figure 6). The pre-irrigation survey (DOY 134) showed a vertical transition from higher to lower resistivity without noticeable anomalies. The observed gradient aligned with the expectation that the predominant ET during the early vegetative stages of maize would be homogeneous surface evaporation of the rainfed soil water, when canopy coverage, root growth, and water uptake were less significant (Figure 1b). Upon irrigation, ERT was able to differentiate the irrigated beds from the exposed and nonirrigated paths in the topsoil.

ERT also highlighted the extent of soil affected by ET in response to irrigation manipulation and the development of maize. During and after the manipulated irrigation period (DOY 187 and 214), ERT showed higher resistivity at the water-stressed T1–T2 than the non-water-stressed T3–T5 at matching depths (Figure 6). Time-lapse ERT also showed a significant increase in resistivity (decrease in estimated SWC) at T1 and T2 between DOY 153 and 214 (Figure 7), and the drying of soil at such depths suggested deeper RWU activities. Maize was found to induce soil drying as deep as 1.6 m when well-watered. When the soil water stress was present in the topsoil, the maximum RWU rate of maize was found to shift deeper, and root length density at depths also increased (Garré et al., 2011; Srayeddin & Doussan, 2009).

During the full irrigation period (DOY 197–229), all treatments received the same amount of irrigation, while ERT showed SWC decreased between DOY 214 and 228 at T3–T5 (irrigation < ET) but increased at T1–T2 (irrigation > ET) (Figure 7). Physiologically, for a 150-day maize planted in April in California, the period between growth days 71–120 (corresponding to DOY 181–230) is its reproductive

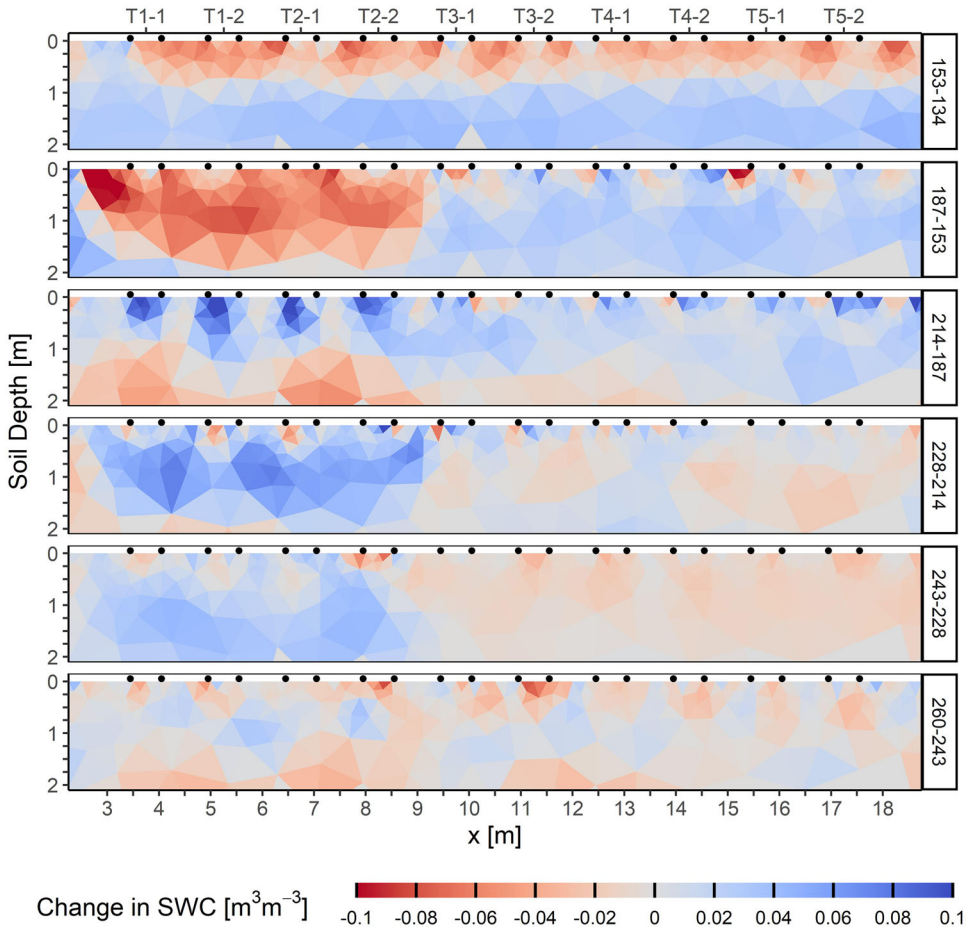

FIGURE 7 Temporal changes in soil water content compared to the previous acquisition. Negative values (red) indicate drying, and positive values (blue) indicate wetting. SWC, soil water content.

stage when kernel development is most active and crop water demand is at its peak (tabs. 11 and 17, and fig. 37 in Allen et al., 1998). The observation of smaller ET at T1 and T2 suggests a state of prolonged and severe soil water stress during the vegetative stages that could trigger physiological adaptation or damage (Cai et al., 2017; Tardieu et al., 2018)—to lower transpiration rate even if the SWC became available. Beyond growth day 121 (i.e., DOY 231), grain filling ceases, maize has reached maturity, and crop water demand decreases linearly from maximum to baseline. Also, no more irrigation was applied during this period. Therefore, the plummeting crop water demand, rather than the recovery of maize at T1 and T2, played a stronger role in the gradual decrease in lateral ΔSWC contrast from DOY 228–260 (Equation 22).

3.3 | Soil water stress and ET

ERT was introduced to spatially analyze soil water stress in the root zone. The one-dimensional approach (such as the method documented in the FAO-56 paper) requires a single estimation of the total water in the rooting depth, therefore assuming that the relevance of RWU and soil water stress is homogeneous in the root zone. However, maize roots were found to have the highest density and contribution to the total RWU near the surface when well-watered (Li et al., 2002). Here, ERT also showed an overall dry-to-wet resistivity gradient despite having the source of irrigation near the surface (Figure 6), indicating a diminishing contribution to the total ET with increasing depths. Under the assumption that RWU decreases with depth, we applied depth-dependent weights when integrating the water stress coefficient in the root zone (Figure 8a).

Vertical water stress profiles showed a persistent reduction of transpiration rate at the top 0.5 m due to low SWC caused by high ET intensities (Figure 8a). During the manipulated irrigation stage (DOY 187), transpiration was inhibited at shallow T1–T2 when SWC approached the wilting point, which prompted deeper RWU activities. The ET reduction coefficients were spatially integrated and fed into the FAO-56 model to compute daily adjusted crop ET ($ET_{c\ adj}$) (Figure 8b–d). The difference between ET adjusted with ERT-based soil water stress at each treatment versus ET without ERT adjustment ($K_r = 1$, $K_s = 1$) was highlighted (Figure 8d).

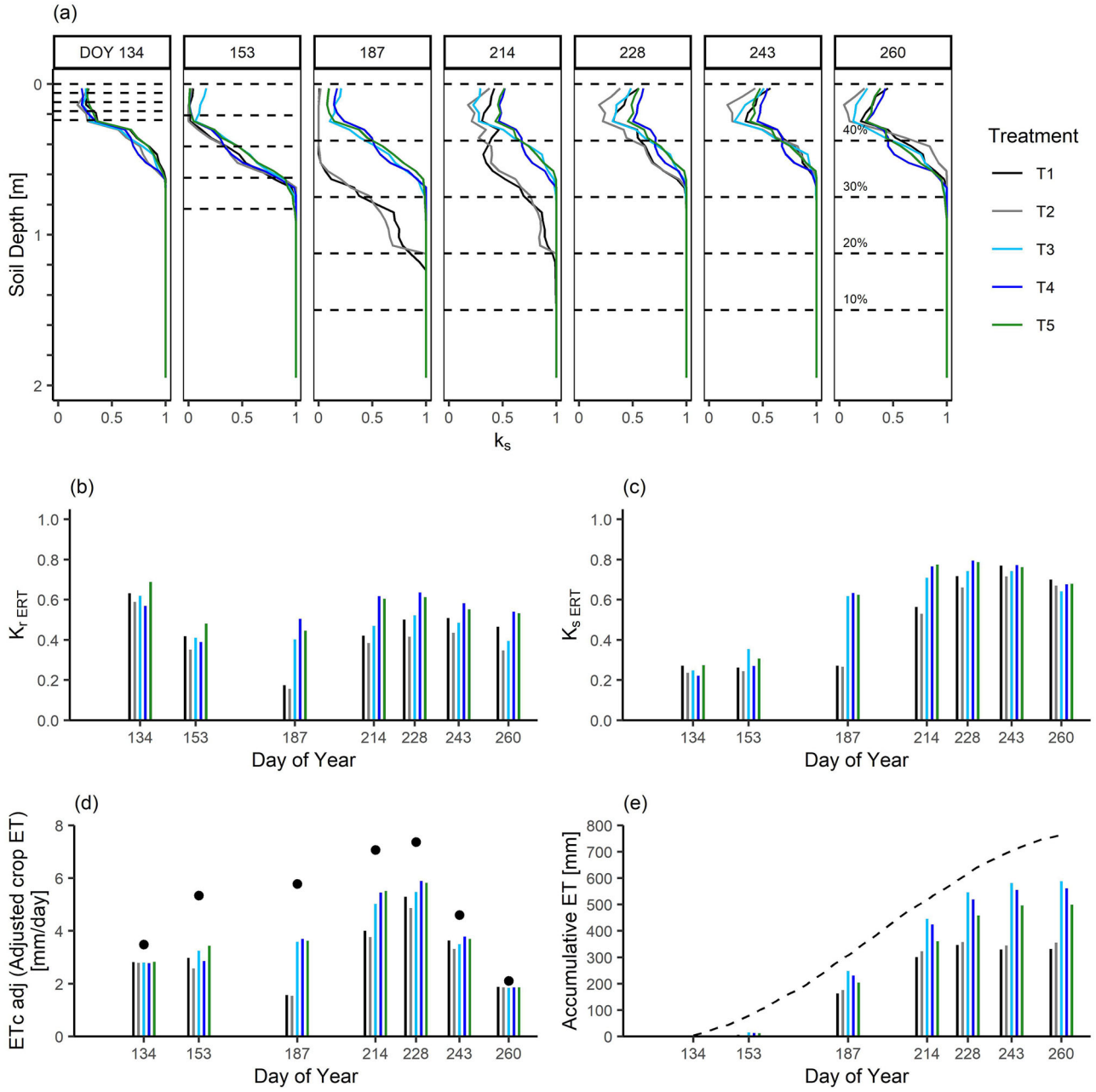

FIGURE 8 (a) Depth profile of local water stress coefficient (k_s). The dotted lines are the four quartiles of the effective rooting depth, labeled with the contribution (%) to the total evapotranspiration (ET). Spatially integrated (b) soil evaporation reduction coefficient $K_{r\,ERT}$ and (c) water stress coefficient $K_{s\,ERT}$. (d) Daily ET from FAO-56 model. The points are the ET values without ERT soil water stress adjustment. (e) Accumulative ET since day of year (DOY) 134 based on soil water content (SWC) mass balance. The dotted line is accumulative ET without electrical resistivity tomography (ERT) soil water stress adjustment.

The accumulative ET calculated based on SWC mass balance showed higher values at the non-water-stressed treatments (Figure 8e), which merely reflected the fact that those treatments received a higher volume of irrigation input. However, we encountered negative ET at T1–T2 toward the end of the growing season, as seen from the slight decrease in acculturative ET values. This issue was also observed by Cassiani et al. (2012), which could be attributed to (1) the different time scale between the dynamic events (i.e., irrigation, ET) and ERT acquisition frequency (Blanchy et al., 2020); (2) smoothing of the resistivity in ERT inversion (Descloitres et al., 2008); and (3) decreasing sensitivity and resolution with depths using surface electrodes (Srayeddin & Doussan, 2009).

3.4 | Limitations and future outlook

Converting soil ER from ERT to soil hydraulic properties based on a universal pedophysical relationship has been challenging. Given a heterogeneous field, multiple calibrations

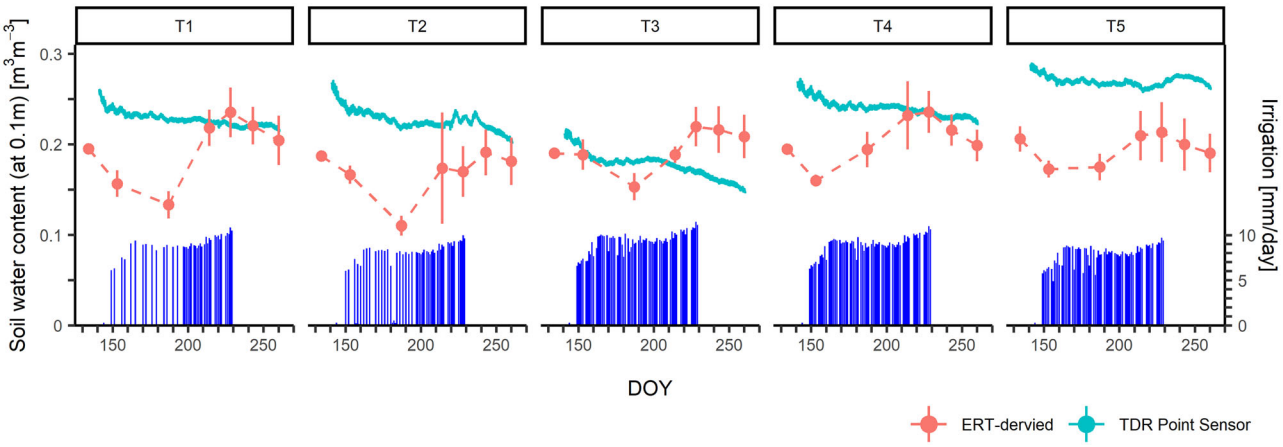

FIGURE 9 Comparison between electrical resistivity tomography (ERT)-derived soil water content (SWC) and time-domain reflectometry (TDR) point SWC measurement at 0.1-m depth. The error bar is the standard deviation of the SWC from ERT mesh cells at matching depths of each treatment. The bar plot (dark blue) is the irrigation volume per day.

would be necessary, which could introduce sharp transitions between the defined boundaries (Garré et al., 2011). An example of heterogeneity would be the compaction at the paths from machinery passages, where soil and pore structures could be heavily modified (Celano et al., 2011; Michot et al., 2003). Hysteresis due to wet–dry cycles was also identified as an issue when the pedophysical relationship was applied during both cycles (Zhou et al., 2001).

How representative the calibration relationship derived from controlled laboratory experiments was in the entire field has been questioned, while the lack of ground truth at matching locations to evaluate the applicability of the calibration was the limitation of this study. Nevertheless, comparing SWC derived from ERT and TDR SWC sensors (5TM, Decagon) (installed at the north end of the plot, not at the ERT transect) at matching depth (0.1 m), we observed that, throughout the growing season, (1) TDR measured higher SWC at water-deficit T1 and T2 than T3, and (2) TDR showed similar trends of decreasing SWC at all treatments, irresponsive to the irrigation manipulation (Figure 9). In this study, the TDR sensors were installed near the end of the irrigation pipelines, where we observed wetter surface soil compared to the rest of the plot. The comparison between point sensors and ERT highlighted the importance of the installation locations and the advantage of ERT thanks to its spatial coverage.

Some potential issues with the assumptions of the ET reduction coefficients ($K_{r,\,ERT}$ and $K_{s,\,ERT}$) are as follows: (1) using a fixed maximum rooting depth and fixed depth-wise contribution to RWU across all treatments did not consider if soil water stress has triggered deeper root development and higher RWU from the deep roots, as observed in time-lapse ERT (Figure 6); and (2) the assumption that the transpiration rate decreased linearly with SWC after a threshold value (θ_{Ks}) and ceased at wilting point, independent of species, has been questioned.

Increasing ERT survey frequency will enable more detailed spatiotemporal analyses that can improve the use of ERT in crop ET computation. With temporally denser ERT datasets, the rate of RWU as a function of depth and time and the accumulative ET over a shorter time frame could be calculated using the SWC mass balance approach. These data can be used to (1) adjust the extent of rooting depth and the contribution of each depth to the total ET, (2) study if prolonged water stress physiologically alters transpiration, and (3) investigate the applicability of SWC thresholds to determine the RWU rate. These objectives will be beneficial to evaluate the performance of the manipulated deficient irrigation, study how prolonged heat and drought may temporally and permanently alter ET patterns, and improve the ET monitoring and modeling capability that better informs water resource management.

AUTHOR CONTRIBUTIONS

Chunwei Chou: Conceptualization; data curation; formal analysis; investigation; methodology; visualization; writing—original; draft; writing—review and editing. **Luca Peruzzo**: Conceptualization; data curation; formal analysis; investigation; methodology; writing—original; draft; writing—review and editing. **Nicola Falco**: Conceptualization; data curation; formal analysis; methodology. **Zhao Hao**: Data curation; formal analysis; methodology. **Benjamin Mary**: writing—review and editing. **Jiannan Wang**: Data curation. **Yuxin Wu**: Conceptualization; data curation; funding acquisition; investigation; methodology; project administration; supervision; writing—review and editing.

ACKNOWLEDGMENTS

Funding for this research was provided by the Laboratory Directed Research and Development (LDRD) grant at the Lawrence Berkeley National Lab (LBNL) and the Watershed Function Scientific Focus Area program funded by the U.S. Department of Energy, Office of Science, Office of Biological and Environmental Research under Award Number DE623AC02-05CH11231. The authors thanked collaborators at Russell Ranch Sustainable Agriculture Facility at UC Davis (Nicole E. Tautges, Taylor Becker, Israel Herrera, Luis Loza, and Kate Scow).

CONFLICT OF INTEREST STATEMENT

The authors declare no conflicts of interest.

DATA AVAILABILITY STATEMENT

Data are published in Data Dryad: https://doi.org/10.7941/D15W4P

ORCID

Chunwei Chou https://orcid.org/0000-0002-9600-4270
Luca Peruzzo https://orcid.org/0000-0002-4065-8910
Benjamin Mary https://orcid.org/0000-0001-7199-2885

REFERENCES

al Hagrey, S. A., Meissner, R., Werban, U., Rabbel, W., & Ismaeil, A. (2004). Hydro-, bio-geophysics. *The Leading Edge*, *23*(7), 670–674. https://doi.org/10.1190/1.1776739

Allen, R. G., Pereira, L. S., Raes, D., & Smith, M. (1998). *Crop evapotranspiration—Guidelines for computing crop water requirements* (Irrigation and Drainage Paper No. 56). Food and Agriculture Organization.

Archie, G. E. (1942). The electrical resistivity log as an aid in determining some reservoir characteristics. *Transactions of the AIME*, *146*(1), 54–61. https://doi.org/10.2118/942054-G

Archontoulis, S., & Licht, M. (2017). *How fast and deep do corn roots grow in Iowa?* Iowa State University Extension and Outreach. https://crops.extension.iastate.edu/cropnews/2017/06/how-fast-and-deep-do-corn-roots-grow-iowa

Ayars, J. E., Phene, C. J., Hutmacher, R. B., Davis, K. R., Schoneman, R. A., Vail, S. S., & Mead, R. M. (1999). Subsurface drip irrigation of row crops: A review of 15 years of research at the water management research laboratory. *Agricultural Water Management*, *42*(1), 1–27. https://doi.org/10.1016/S0378-3774(99)00025-6

Beff, L., Günther, T., Vandoorne, B., Couvreur, V., & Javaux, M. (2013). Three-dimensional monitoring of soil water content in a maize field using electrical resistivity tomography. *Hydrology and Earth System Sciences*, *17*(2), 595–609. https://doi.org/10.5194/hess-17-595-2013

Binley, A., & Kemna, A. (2005). DC resistivity and induced polarization methods. In Y. Rubin & S. S. Hubbard (Eds.), *Hydrogeophysics* (Vol. 50, pp. 129–156). Springer. https://doi.org/10.1007/1-4020-3102-5_5

Blanchy, G., Virlet, N., Sadeghi-Tehran, P., Watts, C. W., Hawkesford, M. J., Whalley, W. R., & Binley, A. (2020). Time-intensive geoelectrical monitoring under winter wheat. *Near Surface Geophysics*, *18*(4), 413–425. https://doi.org/10.1002/nsg.12107

Blundell, R., Schmidt, J. E., Igwe, A., Cheung, A. L., Vannette, R. L., Gaudin, A. C. M., & Casteel, C. L. (2020). Organic management promotes natural pest control through enhanced plant resistance to insects. *Nature Plants*, *6*(5), 483–491. https://doi.org/10.1101/787549

Brillante, L., Bois, B., Mathieu, O., & Lévêque, J. (2016). Electrical imaging of soil water availability to grapevine: A benchmark experiment of several machine-learning techniques. *Precision Agriculture*, *17*(6), 637–658. https://doi.org/10.1007/s11119-016-9441-1

Bussian, A. E. (1983). Electrical conductance in a porous medium. *Geophysics*, *48*(9), 1258–1268. https://doi.org/10.1190/1.1441549

Cai, Q., Zhang, Y., Sun, Z., Zheng, J., Bai, W., Liu, Y., Feng, L., Feng, C., Zhang, Z., Yang, N., Evers, J. B., & Zhang, L. (2017). Morphological plasticity of root growth under mild water stress increases water use efficiency without reducing yield in maize. *Biogeosciences*, *14*(16), 3851–3858. https://doi.org/10.5194/bg-2017-103

Cassiani, G., Ursino, N., Deiana, R., Vignoli, G., Boaga, J., Rossi, M., Perri, M. T., Blaschek, M., Duttmann, R., Meyer, S., Ludwig, R., Soddu, A., Dietrich, P., & Werban, U. (2012). Noninvasive monitoring of soil static characteristics and dynamic states: A case study highlighting vegetation effects on agricultural land. *Vadose Zone Journal*, *11*(3), vzj2011.0195. https://doi.org/10.2136/vzj2011.0195

Celano, G., Palese, A. M., Ciucci, A., Martorella, E., Vignozzi, N., & Xiloyannis, C. (2011). Evaluation of soil water content in tilled and cover-cropped olive orchards by the geoelectrical technique. *Geoderma*, *163*(3–4), 163–170. https://doi.org/10.1016/j.geoderma.2011.03.012

Cimpoiaşu, M. O., Kuras, O., Pridmore, T., & Mooney, S. J. (2020). Potential of geoelectrical methods to monitor root zone processes and structure: A review. *Geoderma*, *365*, 114232. https://doi.org/10.1016/j.geoderma.2020.114232

Descloitres, M., Ribolzi, O., Troquer, Y. L., & Thiébaux, J. P. (2008). Study of water tension differences in heterogeneous sandy soils using surface ERT. *Journal of Applied Geophysics*, *64*(3–4), 83–98. https://doi.org/10.1016/j.jappgeo.2007.12.007

Ernstson, K., & Kirsch, R. (2006). Geoelectrical methods. In R. Kirsch (Ed.), *Groundwater geophysics* (pp. 85–117). Springer. https://doi.org/10.1007/3-540-29387-6_3

Garré, S., Javaux, M., Vanderborght, J., Pagès, L., & Vereecken, H. (2011). Three-dimensional electrical resistivity tomography to monitor root zone water dynamics. *Vadose Zone Journal*, *10*(1), 412–424. https://doi.org/10.2136/vzj2010.0079

Hayashi, M. (2004). Temperature-electrical conductivity relation of water for environmental monitoring and geophysical data inversion. *Environmental Monitoring and Assessment*, *96*, 119–128. https://doi.org/10.1023/B:EMAS.0000031719.83065.68

Hilhorst, M. A. (2000). A pore water conductivity sensor. *Soil Science Society of America Journal*, *64*(6), 1922–1925. https://doi.org/10.2136/sssaj2000.6461922x

Iden, S., & Durner, W. (2014). Comment to "Simple consistent models for water retention and hydraulic conductivity in the complete moisture range" by A. Peters. *Water Resource Research*, *50*(9), 7530–7534. https://doi.org/10.1002/2014WR015937

Kelly, B. F. J., Acworth, R. I., & Greve, A. K. (2011). Better placement of soil moisture point measurements guided by 2D resistivity tomography for improved irrigation scheduling. *Soil Research*, *49*(6), 504–512. https://doi.org/10.1071/SR11145

Kranz, W. L., Irmak, S., van Donk, S. J., Yonts, C. D., & Martin, D. L. (2008). *Irrigation management for corn* (NebGuide G1850).

University of Nebraska Extension. http://extensionpublications.unl.edu/assets/pdf/g1850.pdf

Li, Y., Fuchs, M., Cohen, S., Cohen, Y., & Wallach, R. (2002). Water uptake profile response of corn to soil moisture depletion. *Plant, Cell and Environment*, *25*(4), 491–500. https://doi.org/10.1046/j.1365-3040.2002.00825.x

Losinno, B., & Sainato, C. (2018). Time-lapse electrical resistivity tomography applied to soil infiltration. *Chilean Journal of Agricultural & Animal Sciences*, *34*(3), 243–253. (In Spanish, with English abstract).

Mary, B., Peruzzo, L., Boaga, J., Cenni, N., Schmutz, M., Wu, Y., Hubbard, S. S., & Cassiani, G. (2020). Time-lapse monitoring of root water uptake using electrical resistivity tomography and mise-à-la-masse: A vineyard infiltration experiment. *Soil*, *6*(1), 95–114. https://doi.org/10.5194/soil-6-95-2020

Michot, D., Benderitter, Y., Dorigny, A., Nicoullaud, B., King, D., & Tabbagh, A. (2003). Spatial and temporal monitoring of soil water content with an irrigated corn crop cover using surface electrical resistivity tomography. *Water Resources Research*, *39*(5), 1138. https://doi.org/10.1029/2002WR001581

Michot, D., Dorigny, A., & Benderitter, Y. (2001). Determination of water flow direction and corn roots-induced drying in an irrigated Beauce CALCISOL, using electrical resistivity measurements. *Earth and Planetary Sciences*, *332*(1), 29–36. https://doi.org/10.1016/S1251-8050(00)01498-1

Monteith, J. L. (1965). Evaporation and environment. *Symposia of the Society for Experimental Biology*, *19*, 205–234.

Panissod, C., Michot, D., Benderitter, Y., & Tabbagh, A. (2001). On the effectiveness of 2D electrical inversion results: An agricultural case study. *Geophysical Prospecting*, *49*(5), 570–576. https://doi.org/10.1046/j.1365-2478.2001.00277.x

Parasnis, D. S. (1988). Reciprocity theorems in geoelectric and geoelectromagnetic work. *Geoexploration*, *25*(3), 177–198. https://doi.org/10.1016/0016-7142(88)90014-2

Penman, H. L. (1948). Natural evaporation from open water, bare soil, and grass. *Proceedings of the Royal Society London*, *193A*, 120–145.

Pertassek, T., Peters, A., & Durner, W. (2015). *HYPROP-FIT software user's manual, V.3.0*. METER Group AG.

Peters, A. (2013). Simple consistent models for water retention and hydraulic conductivity in the complete moisture range. *Water Resource Research*, *49*(10), 6765–6780. https://doi.org/10.1002/wrcr.20548

Ritchie, J. T. (1981). Soil water availability. *Plant and Soil*, *58*(1), 327–338. https://doi.org/10.1007/BF02180061

Rücker, C., Günther, T., & Wagner, F. M. (2017). pyGIMLi: An open-source library for modelling and inversion in geophysics. *Computers and Geosciences*, *109*, 106–123. https://doi.org/10.1016/j.cageo.2017.07.011

Samouëlian, A., Cousin, I., Tabbagh, A., Bruand, A., & Richard, G. (2006). Electrical resistivity survey in soil science: A review. *Soil and Tillage Research*, *83*(2), 173–193. https://doi.org/10.1016/j.still.2004.10.004

Schneider, M., & Goss, K.-U. (2012). Prediction of water retention curves for dry soils from an established pedotransfer function: Evaluation of the Webb model. *Water Resources Research*, *48*, W06603, https://doi.org/10.1029/2011WR011049

Srayeddin, I., & Doussan, C. (2009). Estimation of the spatial variability of root water uptake of maize and sorghum at the field scale by electrical resistivity tomography. *Plant and Soil*, *319*(1–2), 185–207. https://doi.org/10.1007/s11104-008-9860-5

Tardieu, F., Simonneau, T., & Muller, B. (2018). The physiological basis of drought tolerance in crop plants: A scenario-dependent probabilistic approach. *Annual Review of Plant Biology*, *69*, 733–759. https://doi/10.1146/annurev-arplant-042817-040218

Topp, G. C., Davis, J. L., & Annan, A. P. (1980). Electromagnetic determination of soil water content: Measurements in coaxial transmission lines. *Water Resources Research*, *16*(3), 574–582. https://doi.org/10.1029/WR016i003p00574

Vanella, D., Ramírez-Cuesta, J., Intrigliolo, D., & Consoli, S. (2019). Combining electrical resistivity tomography and satellite images for improving evapotranspiration estimates of citrus orchards. *Remote Sensing*, *11*(4), 373. https://doi.org/10.3390/rs11040373

Vanella, D., Ramírez-Cuesta, J. M., Sacco, A., Longo-Minnolo, G., Cirelli, G. L., & Consoli, S. (2021). Electrical resistivity imaging for monitoring soil water motion patterns under different drip irrigation scenarios. *Irrigation Science*, *39*(1), 145–157. https://doi.org/10.1007/s00271-020-00699-8

van Genuchten, M. T. (1980). A closed-form equation for predicting the hydraulic conductivity of unsaturated soils. *Soil Science Society of America Journal*, *44*(5), 892–898. https://doi.org/10.2136/sssaj1980.03615995004400050002x

Waxman, M. H., & Smits, L. J. M. (1968). Electrical conductivities in oil-bearing shaly sands. *Society of Petroleum Engineers Journal*, *8*(02), 107–121. https://doi.org/10.2118/1863-A

Werban, U., Al Hagrey, S. A., & Rabbel, W. (2008). Monitoring of root-zone water content in the laboratory by 2D geoelectrical tomography. *Journal of Plant Nutrition and Soil Science*, *171*(6), 927–935. https://doi.org/10.1002/jpln.200700145

Wolf, K. M., Torbert, E. E., Bryant, D., Burger, M., Denison, R. F., Herrera, I., Hopmans, J., Horwath, W., Kaffka, S., Kong, A. Y. Y., Norris, R. F., Six, J., Tomich, T. P., & Scow, K. M. (2018). The century experiment: The first twenty years of UC Davis' Mediterranean agroecological experiment. *Ecology*, *99*(2), 503–503. https://doi.org/10.1002/ecy.2105

Zhou, Q. Y., Shimada, J., & Sato, A. (2001). Three-dimensional spatial and temporal monitoring of soil water content using electrical resistivity tomography. *Water Resources Research*, *37*(2), 273–285. https://doi.org/10.1029/2000WR900284

How to cite this article: Chou, C., Peruzzo, L., Falco, N., Hao, Z., Mary, B., Wang, J., & Wu, Y. (2024). Improving evapotranspiration computation with electrical resistivity tomography in a maize field. *Vadose Zone Journal*, *23,* e20290. https://doi.org/10.1002/vzj2.20290